Silica Polymerization Driving Opposite Effects of pH on Aqueous Carbonation Using Crystalline and Amorphous Calcium Silicates

Hang Zhai,[†,*] Qiyuan Chen,[†] Yan Duan,[‡] Bin Liu,[§] and Bu Wang[†,*]

[†]Department of Civil and Environmental Engineering, University of Wisconsin-Madison, Madison, Wisconsin 53706, United States

[‡]Spin-X Institute, South China University of Technology, Guangzhou 510641, People's Republic of China

[§] National Academy of Agriculture Green Development, College of Resources and Environmental Sciences, China Agricultural University, Beijing 100193, People's Republic of China

[*]**To whom correspondence should be addressed.**

Hang Zhai

Department of Civil and Environmental

Engineering, University of Wisconsin-Madison, Madison, Wisconsin 53706, United States;

orcid.org/0000-0002-8161-448X;

Email: hzhai25@wisc.edu

Bu Wang

Department of Civil and Environmental

Engineering, University of Wisconsin-Madison, Madison, Wisconsin 53706, United States;

orcid.org/0000-0002-9294-0918;

Email: bu.wang@wisc.edu

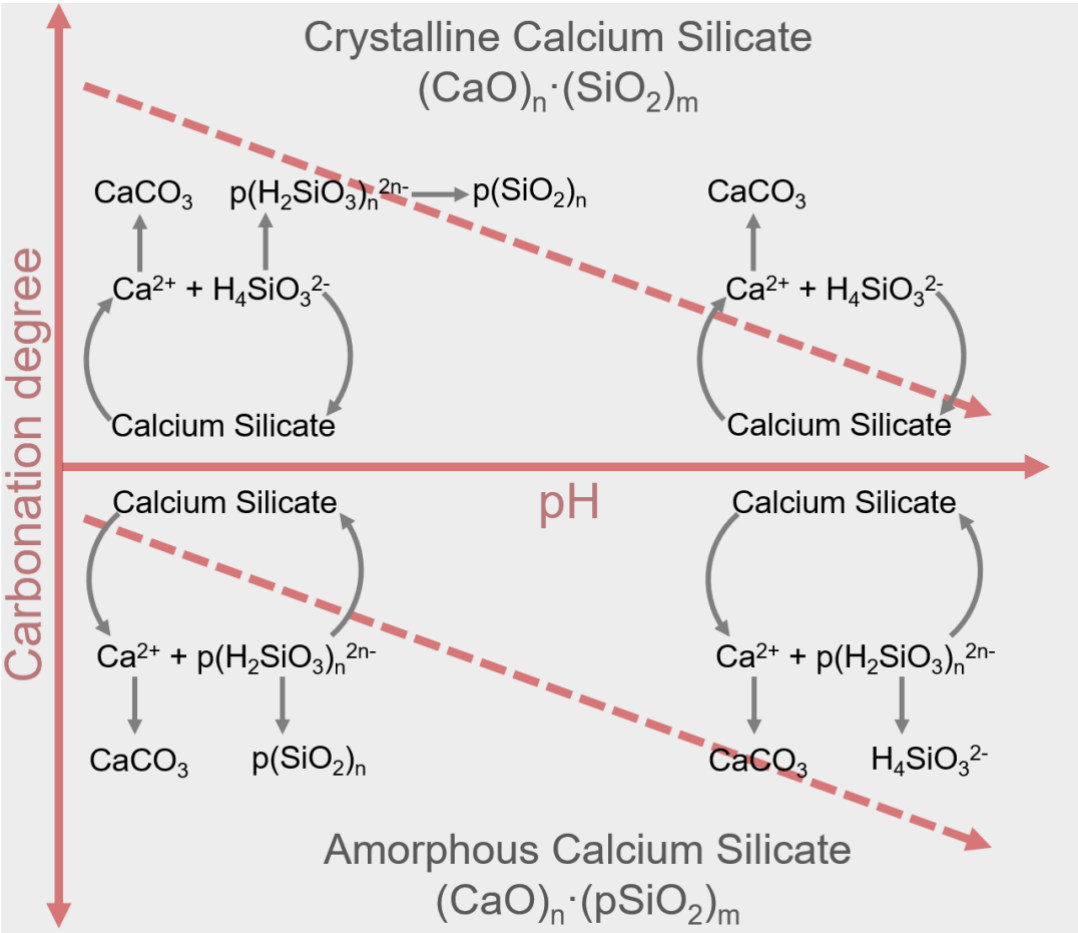

TOC

Synopsis

Calcium silicate, a representative alkaline-earth silicate, has been widely explored in the studies of carbon dioxide (CO_2) mineralization. We conducted a comparison of the pH dependencies of carbonation processes for crystalline calcium silicate (CCS) and amorphous calcium silicate (ACS) under basic conditions–CCS exhibited higher carbonation efficiency at lower pH levels, whereas ACS demonstrated enhanced carbonation under more basic conditions.

Abstract

The aqueous carbonation of calcium silicate (CS), a representative alkaline-earth silicate, has been widely explored in the studies of carbon dioxide (CO_2) mineralization. In this context, we conducted a specific comparison of the carbonation behaviors between the crystalline calcium silicate (CCS) and amorphous calcium silicate (ACS) across a pH range from 9.0 to 12.0. Interestingly, we observed opposite pH dependencies in the carbonation efficiencies (i.e., CaO conversion into $CaCO_3$ in 1 M Na_2CO_3/$NaHCO_3$ solution under ambient conditions) of CCS and ACS—the carbonation efficiency of CCS decreased with increasing the solution basicity while that of ACS showed an inverse trend. In-depth insights were gained through *in situ* Raman characterizations, indicating that these differing trends appeared to originate from the polymerization/depolymerization behaviors of silicates released from minerals. More specifically, higher pH conditions seemed to favor the carbonation of minerals containing polymerized silica networks. These findings may contribute to a better understanding of the fundamental factors influencing the carbonation behaviors of alkaline earth silicates through interfacial coupled dissolution and precipitation processes. Moreover, they offer valuable insights for selecting optimal carbonation conditions for alkaline-earth silicate minerals.

KEYWORDS: CO_2 mineralization, calcium silicates, pH effects, interfacial coupled dissolution and precipitation, crystalline and amorphous phases

1. Introduction.

Mineral carbonation, a process of sequestering carbon dioxide (CO_2) through the formation of stable carbonates, has gained significant attention due to its potential in capturing/storing CO_2 and addressing global climate change.[1–3] In the context of removing CO_2 from the atmosphere, direct air capture can be accomplished using alkaline chemical solvents such as NaOH or KOH (eq. 1).

$$CO_2 + 2OH^- \rightarrow CO_3^{2-} + 2H_2O \quad (CO_2 \text{ capture}) \tag{1}$$

However, significant challenges lie in how to cost-effectively regenerate the hydroxide solution and also how to store the captured CO_2 durably. The storage of CO_2 can be achieved by mineral carbonation,[12–14] which involves physiochemical processes such as adsorption, incorporation, and/or precipitation taking place at the mineral-water interface.[4,5] Among these processes, the precipitation plays a crucial role in the formation of thermodynamically stable carbonates like calcite ($CaCO_3$, $K_{sp} = 4.45 \times 10^{-9}$, K_{sp} is the solubility product constant),[6] dolomite ($CaMg(CO_3)_2$, $K_{sp} = 6.17 \times 10^{-19}$),[7] and siderite ($FeCO_3$, $K_{sp} = 3.15 \times 10^{-11}$),[8] which effectively restricts CO_2 re-emissions from minerals into the atmosphere. Consequently, minerals containing calcium (Ca), magnesium (Mg), and/or iron (Fe) are considered as natural feedstocks for CO_2 sequestration in environmental applications.[9–11]

Recently, we have reported the possibility of regenerate the hydroxide solution through mineral carbonation under basic conditions.[17, 25] This indirect carbonation process involves performing the following reaction at high pH (using calcium silicate as an example mineral):

$$CaSiO_3 + CO_3^{2-} + H_2O \rightarrow CaCO_3 + 2OH^- + SiO_2 \tag{2}$$

In contrast to the direct carbonation approach, where the mineral directly reacts with gaseous CO_2 in one step, the carbonate ions here are provided as a soluble carbonate salt such as Na_2CO_3. Different from the commonly used acidification approach where cations are leached out of the mineral, the acceleration in mineral carbonation (eq. 4) is hypothesized to be that basic solutions convert mineral surfaces into Ca-rich CSH, which is then easily carbonated.[17, 25] The carbonating reaction results in the formation of OH^- (eq. 2) which can be further used to capture CO_2 from atmosphere (eq. 1). Based on these reactions, CO_2 capture and mineralization can be achieved all under basic conditions, without large pH swing or energy-intensive sorbent regeneration.

Unlike mineral carbonation in acidic conditions, indirect carbonation under basic conditions is under researched. L. Monasterio-Guillo et al. conducted carbonation experiments using wollastonite, a crystalline phase of calcium silicate (CS), in $KHCO_3$ (pH 9.4) and K_2CO_3

(pH 12.5) solutions, revealing that the lower pH level led to more $CaCO_3$ formation compared to the higher pH level (21 wt% at pH 9.4 vs. 44 wt% at pH 12.5)).[27] This suggests that a low pH level could lead to a higher carbonation degree, as the solubility of alkali metal silicate (e.g., diopside and forsterite) is lower at higher pH levels.[28] However, in the case of both amorphous CS and coal fly ash (containing significant content of amorphous aluminosilicates) samples, an opposite pH dependence in the basic region was observed, with high carbonation efficiency achieved at high pH levels.[17, 25] We speculated that these different pH dependences of the CS carbonation were attributed to the mineral crystallinity. The crystallinity plays a significant role in mineral chemical and physical characteristics.[29,30] Well-crystallized CS (CCS) minerals, such as wollastonite or pseudowollastonite, exhibit a highly organized atomic structure. They are characterized by four layers, each of which is composed of a layer of ternary ($Si_3O_9^{6-}$) tetrahedral chains and a layer of distorted-bicapped Ca octahedra. This structural organization contributes to higher thermostability and lower solubility compared to its amorphous forms.[31] In contrast, amorphous (glassy) calcium silicate (ACS), mostly presenting as polysilicates, lacks long-range order in their structures.[32,33] While it is well known that the dissolution of crystalline silicates is slower than their amorphous counterparts, different pH dependences in aqueous carbonation behaviors of crystalline and amorphous silicates have not been reported, as far as we are aware.

In this study, our aim was to test the hypothesis that the crystallinity of silicates could influence the pH dependence of mineral carbonation, by conducting a comparison of carbonation processes for CCS and ACS under basic conditions (pH ranging from 9.0 to 12.0). Understanding the interplay between atomic structural features and aqueous carbonation behavior will provide insights into the fundamental mechanisms governing the carbonation of silicate minerals. Such insights are particularly lacking for carbonation under basic conditions. The link between mineralogical features and carbonation performance may also be utilized in practice to inform the selection of optimal carbonation conditions for realistic mineral feedstocks. For instance, crystalline feedstocks such as mafic and ultramafic rocks and amorphous feedstocks such as industrial mineral wastes and basaltic glass may require significantly different pH conditions to achieve the optimal carbonation kinetics. Overall, we believe the findings will facilitate the development of more cost-effective and efficient approaches for CO_2 capture and storage.

2. Materials and methods

2.1 Materials

All reagents used in this study were of analytical grade. Commercial CCS (CAS No.: 10101-39-0) and ACS with a low Ca content (ACS-L; CAS No.: 1344-95-2) were purchased

from Sigma-Aldrich. Moreover, ACS with a high Ca content (ACS-H) was synthesized using a sol-gel method at the room temperature.[34] Specifically, 1 M $CaCl_2$ (Fisher Scientific) was added into 1 M Na_2SiO_3 (Sigma) solution with a Ca/Si molar ratio of 1:1. Following the mixing procedure, the white turbid liquid was yielded in the mixing container and gradually hardened. After 10 min of reaction, all precipitates were isolated and mixed with 100 mL deionized water for 1 h to remove unreacted $CaCl_2$, $Ca(OH)_2$, and/or Na_2SiO_3. Then, the suspension was filtered through a 0.45 μm membrane (Whatman). Collected solid materials were dried at 100 °C for 24 h in an oven (Isotemp Oven model 655F, Fisher Scientific). The physical and chemical characteristics of all CS samples (Figure S2) were identified by scanning electron microscope (SEM, Zeiss/LEO 1530)-energy dispersive X-ray detector (EDS, UltraDry EDS Detector, Thermo Fisher Scientific), X-ray diffraction (XRD, Bruker D8 Discovery), Magic angle spinning-nuclear magnetic resonance spectroscope (MAS-NMR, Bruker Avance III), and thermogravimetric analyzer (TGA, Q500, TA Instruments, Figure S1), which confirms the samples exist in the form of calcium silicates rather than a mixture of calcium oxides and silicas. No uncommon hazards are noted.

2.2 CS carbonation in $NaHCO_3$/Na_2CO_3 solutions

Carbonation experiments were conducted at the room temperature (25 °C) using 15 mL polypropylene sealed tubes (VWR Scientific Inc., USA) with vibration using a vortex mixer (ThermoFisher Scientific). Carbonating solutions were prepared using sodium carbonate (Na_2CO_3) and bicarbonate ($NaHCO_3$) with the original concentration of CO_2 ([Na_2CO_3] + [$NaHCO_3$]) at 1 M. Although higher carbonate concentrations resulted in increased CO_2 storage within carbonated CS (Figure S3), all experiments were conducted with an initial concentration of 1 M since the highest concentration of $NaHCO_3$ was limited to approximately 1.14 M.[35] The 1 M $NaHCO_3$ solution was prepared by sonicating it in an ultrasonic bath (Branson 2510 Ultrasonic Cleaner) to accelerate dissolution and the complete dissolution was confirmed by dynamic light scattering (Figure S4). The pH of solution was adjusted by using different mixing ratios of Na_2CO_3 and $NaHCO_3$ (Figure S5) and the pH measurements were performed using a glass electrode pH meter that calibrated with pH buffers at pH 4.01, 10.01, and 13.0 (Orion Versa Star Pro advanced electrochemistry meter, Thermo Scientific). The solid (CS powders)/liquid (carbonating solution) ratio was kept at 50 g/L by adding 0.5g CS powders into 10 mL well-prepared solutions. The sealed tube vibrates transversely to keep the CS powders well mixed with the solution. After 1 hour carbonation, reacted suspensions were centrifugated (Allegra 25R Centrifuge, Beckman Coulter) at 9000 g for 5 min to separate the liquid and solid phases. The separated sediments were further washed using 10 mL double distilled water (DDW) for three times and dried at 100 °C in an oven for 24 h. Almost all Na_2CO_3 was removed

during the washing step (Figures S6 and 7).

2.3 Solids characterizations

The amount of CaO within CCS/ACS converted to $CaCO_3$ in the sediments was determined through a thermal-degradation approach (Figure S7). The weight loss of the testing material was monitored during the gradual temperature increase from 30 ºC to 1000ºC in a nitrogen environment using TGA. The decomposition of calcium carbonate began at around 550 °C ($CaCO_3 \xrightarrow{heating} CaO + CO_2$ (gas)), allowing it to be distinguished from the decomposition of other residues such as $NaHCO_3$ (~100 °C) and Na_2CO_3 (~850 °C).[36] The CO_2 content in the sample is determined as the weight loss of CO2 between 550-850 °C with respect to the dry sample weight. The distribution of elements within the sediments was analyzed using SEM-EDS. Two samples were observed using SEM and more than three areas were imaged for each sample. Moreover, the surficial Ca/Si atomic ratios were quantified using X-ray photoelectron spectroscopy (XPS, ThermoScientific,USA).[37] In comparison with EDX (detecting ~ 1 μm), XPS (detecting ~10 nm) is a more sensitive and quantitative spectroscopic technique identifying elements covering the sample surfaces.[38] The Ca/Si ratios were calculated by integrating peak areas, which can be used to determine relative contents at mineral surfaces. The newly formed phases within the sediments were identified by XRD and transmission electron microscopy (TEM, FEI Tecnai G2 F30 TWIN 300 kV, EA Fischione Instruments, Inc. USA).[39]

2.4 Solutions analyses

The silica species within the solutions were identified through *in situ* confocal Raman microscopy (HORIBA's LabRAM HR Evolution, France). The experimental parameters for Raman analyses were: 532 nm solid wavelength, 300 μm confocal pinhole, ×10 objective lens, 10 s exposure time, and scanning wavenumber range from 600 to 1500 cm^{-1}.[40] For further quantification, the supernatants were isolated by using centrifuge followed by a 200 nm syringe filtration. The filtrated solutions were acidified and diluted up to 20 times using 0.5 M HNO_3 solutions. The concentrations of dissolved elements were measured using inductively coupled plasma-optical emission spectrometry (ICP-OES, Agilent 5110, USA). All the concentration measurements were triplicated to verify the reliability of analyses and testing procedure in this study.

2.5 PHREEQC simulations

The simulations for each solution listed in Tables S1 and S2 were performed based on the ICP-OES results. PHREEQC Interactive Version 3.3.7.11094 was used to model the

reacting $CaSiO_3$-Na_2CO_3 solutions.[41] Initial solutions were equilibrated to calculate the fractions of species and then the equilibrated solutions were used to calculate the saturation indices with respect to possible Ca- and Si-containing phases. All simulations were performed using the minteq v4 database which was supplemented with thermodynamic data for aragonite ($CaCO_3$), calcite ($CaCO_3$), portlandite ($Ca(OH)_2$), and amorphous silica (SiO_2). These simulations were based on the assumption of complete hydrolytic equilibria with respect to various ions, although achieving this equilibrium state is unlikely due to the relatively short reaction time in the experiments. Therefore, the calculated relative supersaturations of potential precipitates were considered as upper limits and they could be considerably lower.

3. Results and Discussions

3.1 Characterizing calcium silicate samples

Prior to carbonation processes, we conducted a comprehensive characterization of the three distinct types of CS samples to determine their physical and chemical properties. The SEM images of the uncarbonated samples are summarized in Figures S2A, B, and C, showing that all three samples exhibited spherical morphology. The corresponding EDS analyses revealed the presence of Ca, Si, and O elements in all samples without contaminants (Figures S2D, E, and F). The atomic ratios of Ca/Si measured using EDS were found to be 1.20, 0.30, and 1.25 for CCS, ACS-L, and ACS-H, respectively. Their particle sizes were approximately 10 μm (Figure S8). To examine the crystallization characteristics of these CS samples, XRD analyses were performed and the results showed that the main diffraction peaks of CCS appeared at 27.67, 31.93, 36.67, 45.56, and 46.04° (2θ), corresponding to the characteristic crystal facets $(1\bar{3}2)$, $(1\bar{3}4)$, (008), (060), and $(\bar{3}30)$ of pseudowollastonite (α-$CaSiO_3$, JCPDS# 74-0874), respectively (Figures 1A).[27] No peaks were observed in XRD spectra collected from ACS-L and ACS-H samples, indicating that they were amorphous phases (Figures 1B and C).

Since the CS structure is typically characterized by the chemical bonds between Si and non-bridging O (Si-O-Ca) or bridging O (Si-O-Si) atoms,[42] we further characterized the degree of silica polymerization within CS by Q^n (where n represents the number of bridging O atoms connected to the Si) distributions of Si atoms. In our ^{29}Si-MAS-NMR spectra, Q^1, Q^2, Q^3, and Q^4 of CS, locate at -75, -85, -100, and -110 ppm, respectively.[43] The spectrum collected from the CCS sample indicated that it contained predominately Q^1 and Q^2 Si-species (Figure 1D). This finding aligns with the reported CCS structures (Figure S9). The CCS structure consists of three Si tetrahedra sharing two bridging O atoms with the rest of O atoms bonding with Ca atoms.[44] On the other hand, the ACS-L and ACS-H samples contain highly polymerized silicate/silica networks, as indicated by the detection of cross-linked Q^3 and Q^4 species (Figures 1E and F). The degree of polymerization of the silica within CS samples can be assessed by the

ratio of peak areas (calculated by $(Q^3 + Q^4)/(Q^1 + Q^2)$), where a high value indicates a high fraction of fully condensed silicate clusters.[34] The ratios of $(Q^3 + Q^4)$ to $(Q^1 + Q^2)$ were found to be 0, 12.88, and 4.42 for CCS, ACS-L, and ACS-H, respectively (Figures 1D, E and F). This result indicated that the degrees of silica polymerization within CS follows an order of ACS-L > ACS-H > CCS (Figures 1D, E and F). Based on these MAS-NMR analyses, the formulas of CCS and ACS can be simplified as $(CaO)_m \cdot (SiO_2)_n$ and $(CaO)_m \cdot (pSiO_2)_n$ (m and n are numbers, $m \ll n$ for ACS-L; $pSiO_2$ means SiO_2 in a highly polymerized network), respectively.

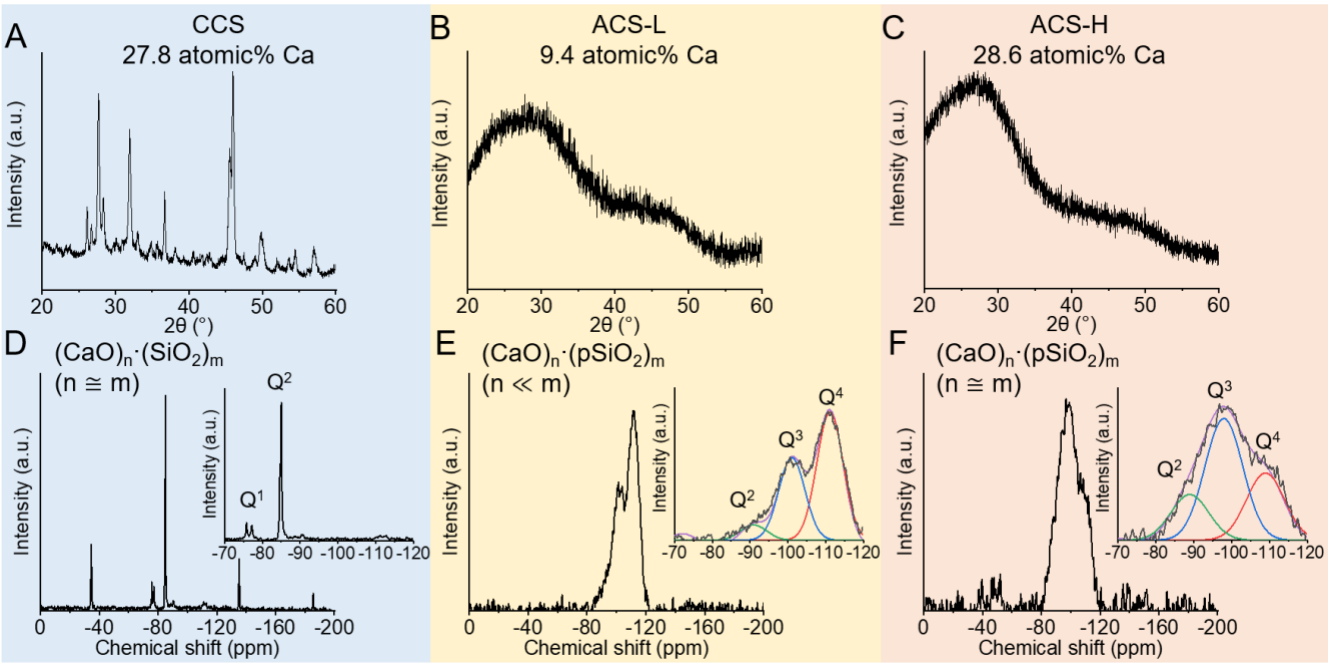

Figure 1. Characterizations of various calcium silicates. (A) XRD peaks at 27.67, 31.93, 36.67, 45.56, and 46.04° (2θ) corresponding to characteristics of crystalline calcium silicates (JCPDS# 74-0874). (B and C) Amorphous phases were confirmed by the presence of two broad humps at approximately 30° and 45° (2θ). ^{29}Si MAS NMR spectra of (D) CCS, (E) ACS-L, and (F) ACS-H. Inset figures in D, E and F are magnified regions of -70 to -120 ppm indicating the presence of four distinct Si-speices including disilicates and chain end groups (Q^1), middle groups in chains (Q^2), chain branching sites (Q^3), and the three-dimensional cross-linked framework (Q^4).

3.2 Quantifying calcium silicate carbonation efficiencies

To quantify the carbonation efficiencies of three types of CS, TGA tests were performed. Figures 2A, B, and C depicted the typical thermogravimetric behaviors of carbonated CS decomposition, showing two prominent mass losses occurring at 100-550 °C (release of H_2O) and 550-850 °C (decomposition of $CaCO_3$). For CCS, increasing pH from 9.0 to 12.0 resulted in a decrease in CO_2 contents within the carbonated products (Figure 2D). In contrast, an increase in CO_2 content was observed with increasing pH values for carbonated ACS samples (Figures 2E and F). This phenomenon indicated the different carbonation

properties between crystalline and amorphous phases. Furthermore, the weight losses of CO_2 were evaluated in terms of the CaO conversion which can serve as an important parameter for assessing the carbonation efficiencies of Ca-containing minerals.[17] Opposite trends of carbonation efficiencies with pH values were also observed between CCS and ACS-L/H samples (Figures 2G, H, and I). Additionally, when comparing the two amorphous phases, ACS-H exhibited higher CaO conversions than that of ACS-L. The higher Ca content in ACS-H might contribute to its enhanced carbonation efficiency.

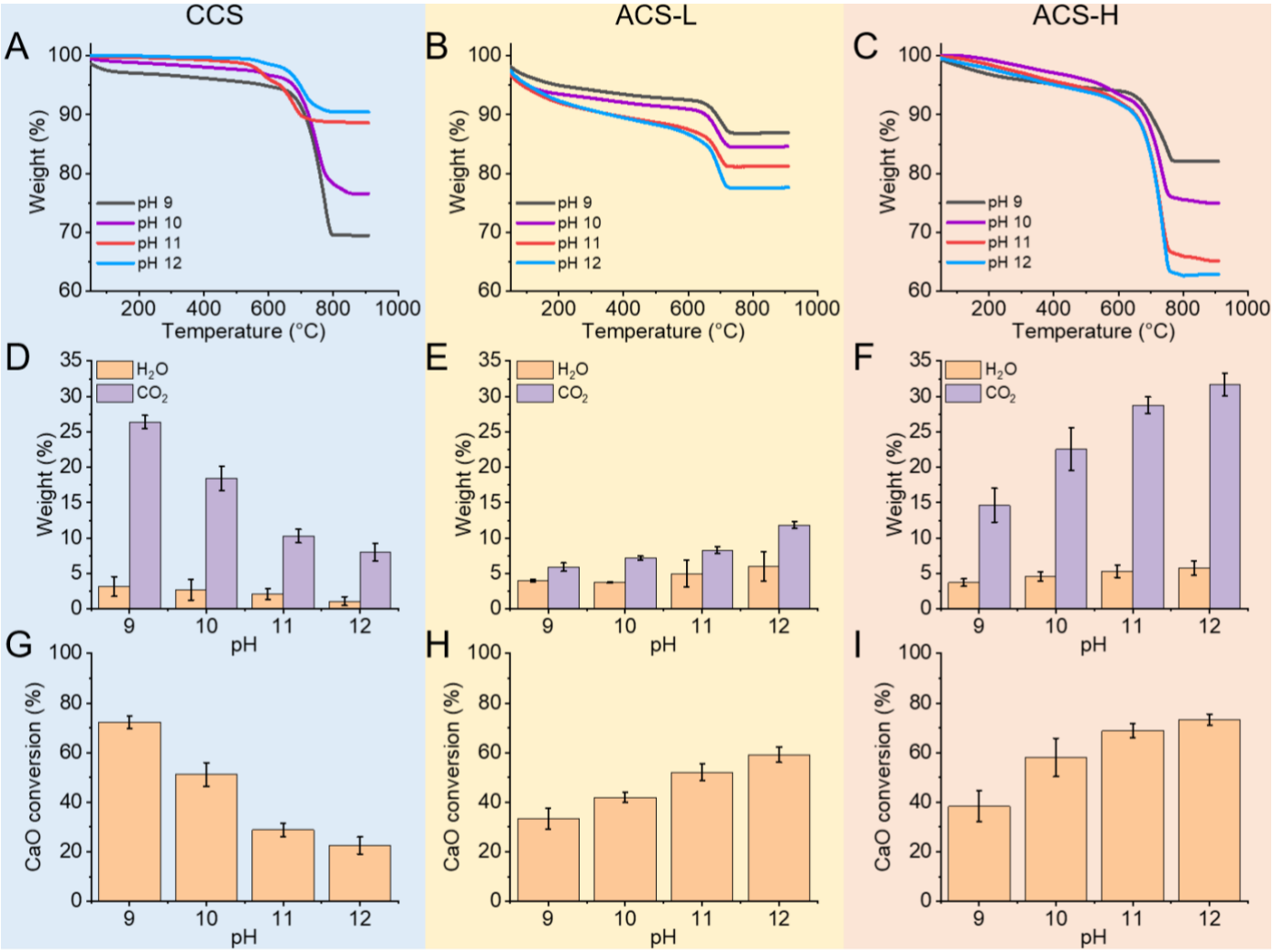

Figure 2. Quantifications of CCS, ACS-L, and ACS-H carbonation efficiencies at various pH values ranging from 9.0 to 12.0. Weight loss curves for (A) CCS, (B), ACS-L, and (C) ACS-H. (D-F) Corresponding H_2O (orange bars) and CO_2 (purple bars) contents derived from TGA weight loss curves. (G-I) Calculated CaO-conversions showing two completely opposite trends with increasing pH of carbonating solutions.

3.3 Characterizing the carbonated CS

To determine their composition of carbonated samples, additional SEM-EDX and high resolution XPS analyses were conducted on the carbonated samples. At pH 9.0, SEM-EDX

analyses of the carbonated CCS showed the formation of SiO_2 (Si-rich areas, Figures 3A1 to A4). When the pH increased to 12.0, no Si-rich aggregates were observed within the carbonated samples (Figures 3B1 to B4). A similar phenomenon was observed in carbonated ACS-L/H samples (Figure S10). In this case, it is reasonable to assume that SiO_2 nucleation was inhibited at pH 12.0 and the EDX-detected Si signals came from the unreacted CS. To verify this hypothesis, surface element analyses using XPS were applied to quantify precipitation of SiO_2 during carbonation processes at various pH levels (Figures 3C1, C2, and C3). The Si2p peak was locked at 102.5 eV and the Ca2p spectra exhibited the expected doublet feature at 346.9 eV (2p3/2) and 350.3eV (2p1/2).[47] These Ca2p peak positions correspond to a divalent oxidation state (Ca^{2+}-O) in inorganic calcium oxygen compounds. The ratios of Ca/Si after carbonation resulted from dissolution and precipitation of secondary minerals including calcium carbonate, silica, and calcium silicate hydrate (CSH). Based on the peak area ratios between Ca and Si signals, the Ca/Si atomic ratios on the mineral surfaces decreased after the carbonation at pH 9.0 for all carbonated CS samples (Figure 3C4). On the other hand, the Ca/Si ratios increased after carbonation at pH 12.0, indicating the formation of different product layers at various pH levels. For CCS from pH 9.0 to 12.0, because less $CaCO_3$ was formed during the carbonation (Figure 2A), an increase in Ca/Si ratio with the rise in pH (Figure 3C4) could be attributed to the dissolution of SiO_2. However, in the carbonated ACS samples, increasing pH resulted in more $CaCO_3$ precipitation (Figure 2B and C), thus, the increase of Ca/Si ratio at high pH values can be attributed to the formation of more $CaCO_3$ and/or release of SiO_2.

Furthermore, the carbonated samples were analysed using XRD for determining their compositions. Collected results indicated that calcite was the dominant crystalline phase among the products after carbonation processes (Figures 4A, B, and C). To thoroughly assess the distribution of crystalline phases, high resolution TEM was performed to directly observe the newly formed product layers at the nanoscale. At pH 9.0 (Figure 4D), a small area with distinct crystalline phases (area 1, Figure 4E1) was observed within an amorphous matrix phase (area 2, Figure 4E2). The best match for the phase in area 2 was identified as calcite, with a measured value of 3.03 Å matching with 3.05 Å for the characteristic d-spacing of (104) planes in the JCPDF database (#86-2341). In contrast, at pH 12.0, more crystalline phases were observed (Figure 4F). The identified phases were calcite and aragonite (Figures 4G1 and G2). In contrast to the observations at pH 9.0, we noted fewer amorphous matrix phases at pH 12.0. These direct observations indicate that highly alkaline conditions promote the formation of crystalline calcium carbonate phases. This phenomenon also suggested that the nucleation of SiO_2 was inhibited under more basic conditions. These findings from TEM at the nanoscale were consistent with the SEM observations and the analyses we performed based on XPS.

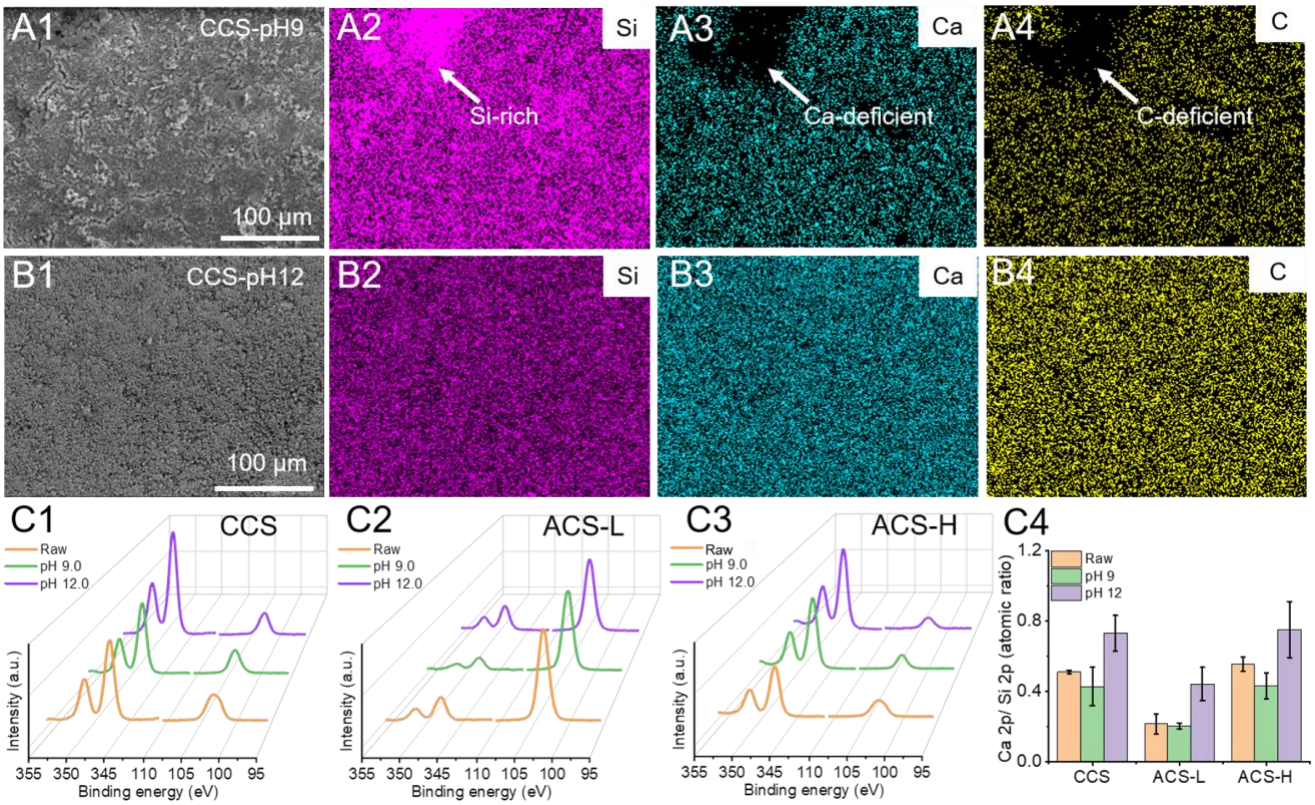

Figure 3. Elemental analyses of carbonated samples at various pH levels ranging from 9.0 to 12.0. (A1) A representative SEM image of carbonated CCS at pH 9.0 and corresponding (A2) Si, (A3) Ca, and (A4) C elemental distributions. SEM images were captured at a resolution of 2048 × 1536 pixels, while EDS mapping images were acquired at a resolution of 512 × 384 pixels. As such, some morphological features (e.g., the cracks in A1) were not observed in the EDS maps. Arrows in A2, A3, and A4 indicate Si-rich areas where Ca and C are depleted. (B1-B4) A representative SEM image and corresponding EDS elemental maps of carbonated CCS at pH 12.0. High-resolution XPS spectra of Ca 2p (346.9 and 350.3 eV) and Si 2p (102.5 eV) at the surface of (C1) CCS, (C2) ACS-L, and (C3) ACS-H samples. (C4) XPS data showing that the Ca/Si ratio on the mineral surface decreased and increased after carbonation at pH 9.0 and 12.0 respectively comparing to the raw sample.

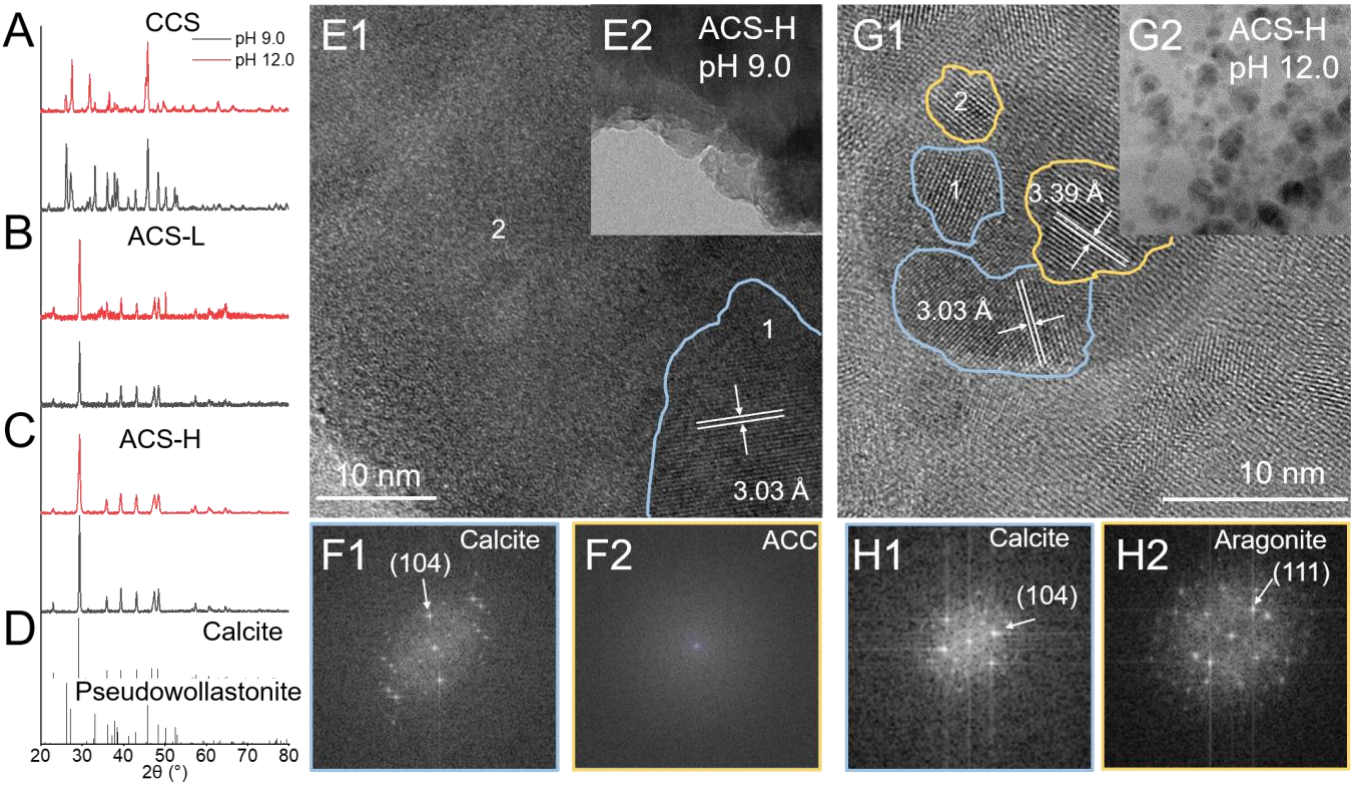

Figure 4. Identification of crystalline phases within the carbonated samples. XRD spectra of carbonated (A) CCS, (B) ACS-L, and (C) ACS-H samples at pH 9.0 (black) and 12.0 (red). (D) Reference peaks of standard calcite (JCPDF #86-2341) and pseudowollastonite (JCPDF #74-0874) (E1) High resolution TEM image of carbonated ACS-H samples at pH 9.0 taken from E2. Corresponding FFT patterns of (F1) areas 1 and (F2) 2, showing the presence of the mixed amorphous and crystalline phases. (G1) High resolution TEM image of carbonated ACS-H samples at pH 12.0 taken from G2. Corresponding FFT patterns of (H1) areas 1 and (H2) 2 demonstrate the presence of calcite and aragonite. The TEM images revealed the presence of aragonite nanocrystals. Aragonite was not detected in A-C, suggesting its content might be below the detection limit of XRD.

3.4 Dissolution properties of CCS and ACS under alkaline conditions.

The dissolution of CS in carbonating solutions provides a sustained source of Ca^{2+} ions, which can initiate the nucleation and growth of calcium carbonates. Therefore, it is reasonable to relate the CS dissolution with its carbonation processes. The dissolution behaviour of CS has been established in previous studies.[48,49] An ion-exchange model presumes that its dissolution proceeds through the solid-state diffusion of protons (H^+) from the solution into silicates, where they produce silanol groups (Si-OH) by the exchange with Ca^{2+} diffusing out of the CS. However, this mechanism is unlikely under strongly basic conditions. Recent observations were in full agreement with the notion of an interfacial coupled dissolution and precipitation process that CS released Ca^{2+} and SiO_3^{2-} into solutions and supersaturated H_4SiO_4/SiO_2 reprecipitates at the mineral-water interfaces.

Here, to in situ investigate the dissolution of CCS and ACS, we applied Raman

spectroscopy. At pH 9.0, Raman peaks located at 1017, 1066, and 1359 cm^{-1} correspond to the ν_5(C–OH) vibration of the HCO_3^-, $\nu_1(CO_3)$ symmetric stretching of CO_3^{2-}, and the CO_2 symmetric stretch (Figure 5A1).[50] At pH 12.0, only CO_3^{2-}-related symmetric stretching was detected, indicating that most CO_2 and/or HCO_3^- converted to CO_3^{2-} (Figure 5A1). For the Si-species, Raman peaks located at 780 cm^{-1} corresponded to the Si-O symmetric stretching of monosilicates ($H_2SiO_4^{2-}$, Figure 5A2).[50,51] Here, we detected Si signals in the extracted solutions via Raman (Figures 5A1 and A2), demonstrating that the dissolution of CS proceeded via an interfacial coupled dissolution and precipitation process rather than solid-state diffusion at pH ranging from 9.0 to 12.0. In both cases of CCS carbonation at pH 9.0 and 12.0, Raman peaks from 750 to 800 cm^{-1} were observed, indicating the presence of monosilicates (Figure 5A2). Because CCS consists of Si tetrahedra rather than polymerized silica (Figure 1D), most likely, these monosilicates could be released directly as part of the dissolution of CCS solids. In this case, the dissolution of CCS in the carbonating solutions can be described as

$$(CaO)_m \cdot (SiO_2)_m + m\,H_2O \xrightarrow{\text{dissolution}} m\,Ca^{2+} + m\,H_2SiO_4^{2-} \tag{5}$$

In contrast, no Raman peaks at ~780 cm^{-1} were observed in the ACS (including ACS-L and ACS-H)-Na_2CO_3/$NaHCO_3$ reacting solutions at pH 9.0 (Figure 5B), indicating that the concentration of monosilicates was relatively lower in solutions. This could be attributed to the highly polymerized nature of original Si-species within ACS-L and ACS-H samples (Figures 1H and I). As the pH values increased, the signal intensity of monosilicates gradually increased (Figure 5C), suggesting that more basic conditions promoted the depolymerization of $pSiO_2$ into monosilicates. To investigate the kinetics of CS dissolution at pH 12.0, we conducted a real-time analysis of the released Si-species. As time progressed, an increasing amount of Si-species was detected in both CCS and ACS-carbonating solutions, with ACS-H exhibiting a faster dissolution rate than CCS (Figure 5D). In the case of CCS, the presence of $H_2SiO_4^{2-}$ was detected within 15 minutes (Figure 5E), while it was not observed in the case of ACS-H (Figure 5F). This suggests that the dissolution of ACS-H proceeds via an incongruent dissolution, releasing $(pSiO_2)n$ rather than $H_2SiO_4^{2-}$. Consequently, we proposed that ACS-H dissolution can occur through the following reactions (eqs. 6 and 7).

$$(CaO)_m \cdot (pSiO_2)_m + m\,H_2O \xrightarrow{\text{dissolution}} m\,Ca^{2+} + (pH_2SiO_4)_m^{2-} \tag{6}$$

$$(pSiO_2)_n + 2n\,OH^- \xrightarrow{\text{depolymerization}} n\,H_2SiO_4^{2-} \quad \text{(at pH 12.0)} \tag{7}$$

In this scenario, ACS, which contains more polymerized Si-species (Figures 1E and F), initially releases $(pSiO_2)_m$ during its dissolution (eq. 6). Subsequently, these released polymerized phases can further depolymerize into monosilicates under highly alkaline conditions (eq. 7). This kind of dissolution, proceeding first via particle detachment rather than ion-by-ion detachment into a surrounding solvent, has been observed in both compact rhombohedra and mesocrystals of coaligned nanoparticle.[52] Even though no direct observation of $pSiO_2$ particles released from dissolving CS solids, we further characterized CS dissolution via quantifying the released Ca^{2+} ions and dissolved silicas/silicates ($dSiO_2$; including SiO_3^{2-}, $HSiO_3^-$, H_2SiO_3, and short-chain SiO_2) in solutions at various pH levels. The results showed that fewer Ca^{2+} ions were released from CCS as pH increased while more basic conditions benefited the decalcification of both ACS-L and ACS-H samples (Figures 6A, B, and C). Similar trends were observed in the cases of $dSiO_2$ (Figures 6D, E, and F). These results indicated that increasing pH from 9.0 to 12.0 accelerated the dissolution of ACS, rather than CCS. This different dissolution properties between CCS and ACS could be the reason for the opposite effects of pH on their aqueous carbonation processes.

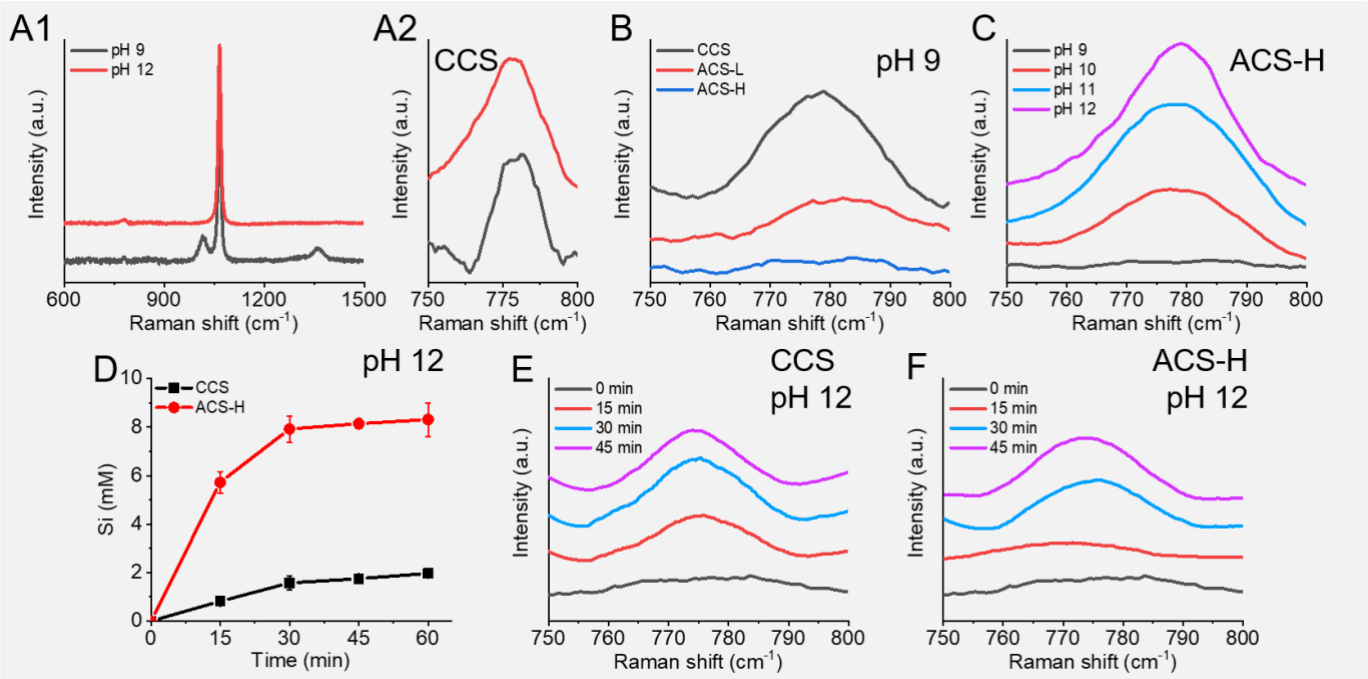

Figure 5. Characterizations of CCS and ACS dissolutions. (A1) Representative Raman spectra collected from CCS-$NaHCO_3$/Na_2CO_3 reacting systems and (A2) their magnified regions of 750 to 800 cm^{-1} assigned to monosilicates at 780 cm^{-1}. (B) Raman spectra collected from CCS (black), ACS-L (red), and ACS-H (blue) carbonation systems indicating the presence of monosilicates only during the CCS carbonation. (C) Raman spectra of ACS-L-$NaHCO_3$/Na_2CO_3 reacting solutions at various pH from 9.0 to 12.0 showing that increasing pH induced the production of monosilicates. (D-F) Kinetics of CCS and ACS-H dissolution at pH 12. (D) The amounts of released Si-containing phases at different time. Time sequence of Raman spectra collected from (E) CCS and (F) ACS-H carbonating solutions at pH 12.

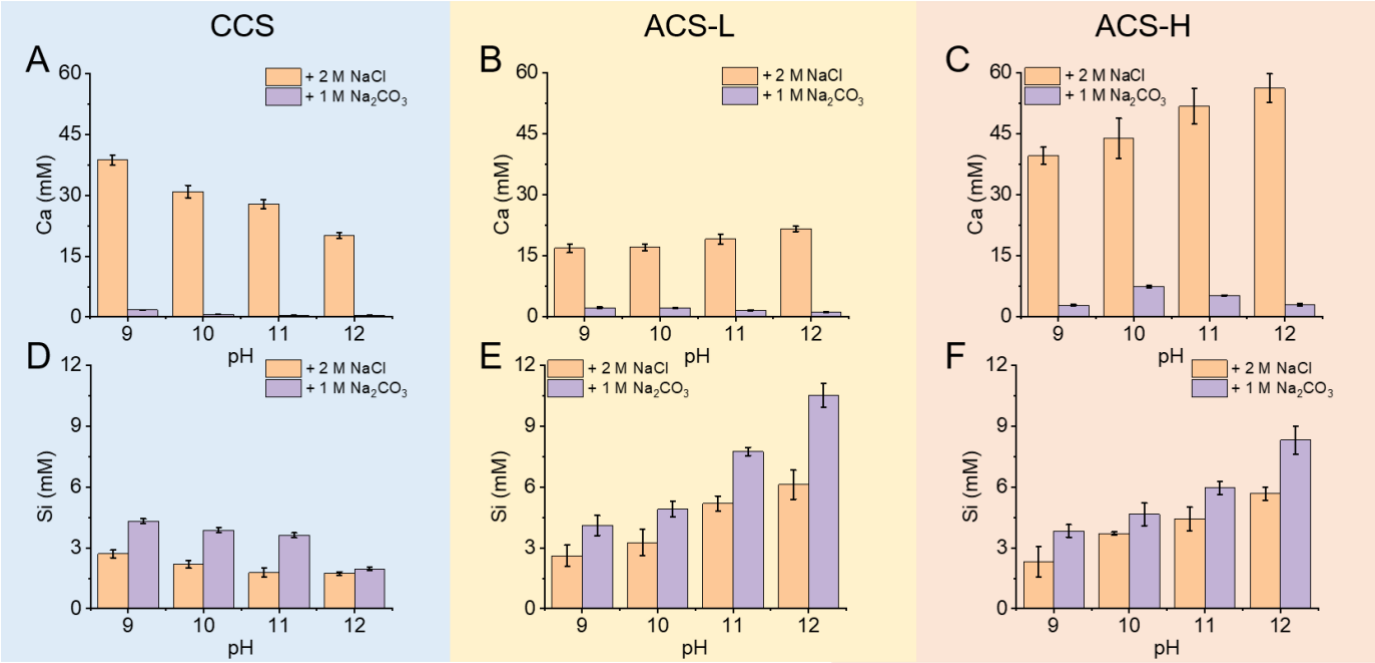

Figure 6. Quantification of released Ca^{2+} from (D) CCS, (E) ACS-L, and (F) ACS-H in the presence of 2 M NaCl (orange bars) and 1 M Na_2CO_3 (purple bars). (G-I) Corresponding amounts of released Si-containing phases measured by ICP-OES.

3.5 Secondary Phase Precipitation During the CCS and ACS carbonation.

The dissolution of CCS proceeded by releasing Ca^{2+} and $H_2SiO_4^{2-}$ ions (depending on pH, Figures S11). Subsequently, the released Ca^{2+} ions were precipitated into $CaCO_3$ during carbonation processes. For the released Si, according to PHREEQC simulations (Table S1 and S2) and also suggested by SEM observations (Figure 3A1), nucleation and precipitation of silica could occur via $H_2SiO_4^{2-}$ polymerization at pH 9.0 (eq .8).

$$m\ H_2SiO_4^{2-} + 2m\ H^+ \xrightarrow{\text{polymerization}} (pSiO_2)_m + 2m\ H_2O \qquad (8)$$

Newly precipitated silica layers at the CS surface have been demonstrated not to be a diffusion barrier for aqueous species, suggesting that Ca^{2+} can still be released from minerals and react with carbonate at mineral surfaces.[53] The consumption of $H_2SiO_4^{2-}$ in the solution will decrease the activity product of $[Ca^{2+}]$ and $[H_2SiO_4^{2-}]$, contributing to more CCS dissolving. At pH 12.0, Si-species are negatively charged (Figure S11) and have a high affinity for Ca^{2+} ions, resulting in fewer Ca^{2+} ions released from original minerals (Figures 6A and D) and converted into $CaCO_3$. In this case, the carbonation degree of CCS decreased with increasing pH (Figure 2G). In contrast, for the case of ACS, the dissolution proceeded by releasing $(pH_2SiO_4)_m^{2-}$ first (eq. 6). At pH 12.0, $(pH_2SiO_4)_m^{2-}$ further depolymerized to $H_2SiO_4^{2-}$ (Figure 5F), resulting in a decrease in the activity product of $[Ca^{2+}]$ and $[(pH_2SiO_4)_m^{2-}]$. Newly formed $H_2SiO_4^{2-}$ could react with Ca^{2+} to form CSH. However, we used a high concentration of carbonates (1 M) which

could reduce the effect of precipitation of CSH. Thus, the relatively high pH level promoted ACS carbonation processes by facilitating the dissolution of ACS and the subsequent precipitation of $CaCO_3$.

4. Conclusion.

In this study, we tested the carbonation behaviors of CCS and ACS under varying pH levels in the basic region. Notably, CCS exhibited higher carbonation efficiency at lower pH levels, whereas ACS demonstrated enhanced carbonation under more basic conditions. The *In situ* Raman spectroscopy provided insights into the underlying mechanisms. For CCS, the release of monosilicates into the carbonating solutions during carbonation was observed, and the lower pH conditions facilitated silica precipitation, leading to monosilicate consumption and subsequent CCS dissolution, thereby enhancing carbonation efficiency. Conversely, ACS contains highly polymerized silicates/silicas. Under highly alkaline conditions, thermodynamic favorability for polysilicate depolymerization occurred, promoting ACS dissolution and explaining the observed pH dependent efficiency. The pH dependence of dissolution behaviors of CCS and ACS in the absence of carbonation supported these findings. Overall, the pH dependence of CS carbonation were influenced by the dissolution behavior of the silica network in the minerals, specifically its degree of polymerization. This understanding has implications for selecting optimal conditions for alkaline earth minerals in the basic pH range.

ASSOCIATED CONTENT

Supporting Information. The Supporting Information is available free of charge on the ACS Publications website.

PHREEQC simulations; SEM images; EDX spectra, thermogravimetric analyses; pH monitoring; X-ray photoelectron spectroscopy; carbonation efficiency; particle size determined by dynamic light scattering; crystal structure of calcium silicates; SEM-EDX mapping; characterizations of SiO_2/CO_2-species.

AUTHOR INFORMATION

Corresponding Authors

Hang Zhai − *Department of Civil and Environmental Engineering, University of Wisconsin-Madison, Madison, Wisconsin 53706, United States*; orcid.org/0000-0002-8161-448X; Email: hzhai25@wisc.edu

Bu Wang − *Department of Civil and Environmental Engineering, University of Wisconsin-*

Madison, Madison, Wisconsin 53706, United States; orcid.org/0000-0002-9294-0918; Email: bu.wang@wisc.edu

Authors

Qiyuan Chen – *Department of Civil and Environmental Engineering, University of Wisconsin-Madison, Madison, Wisconsin 53706, United States*; *Department of Materials Science and Engineering, University of Wisconsin-Madison, Madison, Wisconsin 53706, United States*

Yan Duan − *Spin-X Institute, South China University of Technology, Guangzhou 510641, People's Republic of China*

Bin Liu − *National Academy of Agriculture Green Development, College of Resources and Environmental Sciences, China Agricultural University, Beijing 100193, People's Republic of China*

Notes

The authors declare no competing financial interest.

ACKNOWLEDGEMENTS

This material is based upon work supported by the National Science Foundation under grant no. 2132022. The information, data, or work presented herein were funded in part by the Advanced Research Projects Agency-Energy (ARPA-E), U.S. Department of Energy, under Award Number DE-AR 0001636. The authors gratefully acknowledge use of facilities and instrumentation supported by NSF through the University of Wisconsin Materials Research Science and Engineering Center (DMR-2309000).

REFERENCE

(1) Sanna, A.; Uibu, M.; Caramanna, G.; Kuusik, R.; Maroto-Valer, M. M. A Review of Mineral Carbonation Technologies to Sequester CO2. *Chem. Soc. Rev.* **2014**, *43* (23), 8049–8080. https://doi.org/10.1039/c4cs00035h

(2) Romanov, V.; Soong, Y.; Carney, C.; Rush, G. E.; Nielsen, B.; O'Connor, W. Mineralization of Carbon Dioxide: A Literature Review. *ChemBioEng Rev.* **2015**, *2* (4), 231–256. https://doi.org/10.1002/cben.201500002

(3) Snæbjörnsdóttir, S.; Sigfússon, B.; Marieni, C.; Goldberg, D.; Gislason, S. R.; Oelkers, E. H. Carbon Dioxide Storage through Mineral Carbonation. *Nat. Rev. Earth Environ.* **2020**, *1* (2), 90–102. https://doi.org/10.1038/s43017-019-0011-8

(4) Wang, L.; Putnis, C. V.; Putnis, C. V. Dissolution and Precipitation Dynamics at

Environmental Mineral Interfaces Imaged by in Situ Atomic Force Microscopy. *Acc. Chem. Res.* **2020**, *53* (6), 1196–1205. https://doi.org/10.1021/acs.accounts.0c00128

(5) Liu, W.; Teng, L.; Rohani, S.; Qin, Z.; Zhao, B.; Xu, C. C.; Ren, S.; Liu, Q.; Liang, B. CO2 Mineral Carbonation Using Industrial Solid Wastes: A Review of Recent Developments. *Chem. Eng. J.* **2021**, *416* (February), 129093. https://doi.org/10.1016/j.cej.2021.129093

(6) Hawkes, S. J. What Should We Teach Beginners about Solubility and Solubility Products? *J. Chem. Educ.* **1998**, *75* (9), 1179–1181. https://doi.org/10.1021/ed075p1179

(7) Bénézeth, P.; Berninger, U. N.; Bovet, N.; Schott, J.; Oelkers, E. H. Experimental Determination of the Solubility Product of Dolomite at 50–253 °C. *Geochim. Cosmochim. Acta* **2018**, *224*, 262–275. https://doi.org/10.1016/j.gca.2018.01.016

(8) Bénézeth, P.; Dandurand, J. L.; Harrichoury, J. C. Solubility Product of Siderite (FeCO3) as a Function of Temperature (25-250 °C). *Chem. Geol.* **2009**, *265* (1–2), 3–12. https://doi.org/10.1016/j.chemgeo.2009.03.015

(9) Zhang, D.; Ghouleh, Z.; Shao, Y. Review on Carbonation Curing of Cement-Based Materials. *J. CO2 Util.* **2017**, *21* (June), 119–131. https://doi.org/10.1016/j.jcou.2017.07.003

(10) Eikeland, E.; Blichfeld, A. B.; Tyrsted, C.; Jensen, A.; Iversen, B. B. Optimized Carbonation of Magnesium Silicate Mineral for CO2 Storage. *ACS Appl. Mater. Interfaces* **2015**, *7* (9), 5258–5264. https://doi.org/10.1021/am508432w

(11) Pullin, H.; Bray, A. W.; Burke, I. T.; Muir, D. D.; Sapsford, D. J.; Mayes, W. M.; Renforth, P. Atmospheric Carbon Capture Performance of Legacy Iron and Steel Waste. *Environ. Sci. Technol.* **2019**, *53* (16), 9502–9511. https://doi.org/10.1021/acs.est.9b01265.

(12) Loring, J. S.; Thompson, C. J.; Wang, Z.; Joly, A. G.; Sklarew, D. S.; Schaef, H. T.; Ilton, E. S.; Rosso, K. M.; Felmy, A. R. In Situ Infrared Spectroscopic Study of Forsterite Carbonation in Wet Supercritical CO 2. *Environ. Sci. Technol.* **2011**, *45* (14), 6204–6210. https://doi.org/10.1021/es201284e

(13) Vance, K.; Falzone, G.; Pignatelli, I.; Bauchy, M.; Balonis, M.; Sant, G. Direct Carbonation of Ca(OH)2 Using Liquid and Supercritical CO2: Implications for Carbon-Neutral Cementation. *Ind. Eng. Chem. Res.* **2015**, *54* (36), 8908–8918. https://doi.org/10.1021/acs.iecr.5b02356

(14) Min, Y.; Li, Q.; Voltolini, M.; Kneafsey, T.; Jun, Y. S. Wollastonite Carbonation in Water-Bearing Supercritical CO2: Effects of Particle Size. *Environ. Sci. Technol.* **2017**, *51* (21), 13044–13053. https://doi.org/10.1021/acs.est.7b04475.

(15) Teir, S.; Eloneva, S.; Zevenhoven, R. Production of Precipitated Calcium Carbonate from Calcium Silicates and Carbon Dioxide. Energy Convers. Manag. 2005, 46 (18–19), 2954–2979. https://doi.org/10.1016/j.enconman.2005.02.009

(16) Wang, J.; Watanabe, N.; Inomoto, K.; Kamitakahara, M.; Nakamura, K.; Komai, T.; Tsuchiya, N. Sustainable Process for Enhanced CO2 Mineralization of Calcium Silicates Using a Recyclable Chelating Agent under Alkaline Conditions. J. Environ. Chem. Eng. 2022, 10 (1), 107055. https://doi.org/10.1016/j.jece.2021.107055

(17) Ragipani, R.; Sreenivasan, K.; Anex, R. P.; Zhai, H.; Wang, B. Direct Air Capture and Sequestration of CO_2 by Accelerated Indirect Aqueous Mineral Carbonation under Ambient Conditions. *ACS Sustain. Chem. Eng.* **2022**, *10* (24), 7852–7861. https://doi.org/10.1021/acssuschemeng.1c07867

(18) Zajac, M.; Lechevallier, A.; Durdzinski, P.; Bullerjahn, F.; Skibsted, J.; Ben Haha, M. CO2 Mineralisation of Portland Cement: Towards Understanding the Mechanisms of Enforced Carbonation. *J. CO2 Util.* **2020**, *38* (November 2019), 398–415. https://doi.org/10.1016/j.jcou.2020.02.015.

(19) Plattenberger, D. A.; Ling, F. T.; Tao, Z.; Peters, C. A.; Clarens, A. F. Calcium silicate crystal structure impacts reactivity with CO2 and precipitate chemistry. *Environ. Sci. Technol. Lett.*, **2018**, *5*(9), 558-563. https://doi.org/10.1021/acs.estlett.8b00386

(20) Vanderzee, S.; Zeman, F. Recovery and Carbonation of 100% of Calcium in Waste Concrete Fines: Experimental Results. *J. Clean. Prod.* **2018**, *174*, 718–727. https://doi.org/10.1016/j.jclepro.2017.10.257

(21) Teir, S.; Eloneva, S.; Zevenhoven, R. Production of Precipitated Calcium Carbonate from Calcium Silicates and Carbon Dioxide. *Energy Convers. Manag.* **2005**, *46* (18–19), 2954–2979. https://doi.org/10.1016/j.enconman.2005.02.009

(22) Yang, S.; Mo, L.; Deng, M. Effects of Ethylenediamine Tetra-Acetic Acid (EDTA) on the Accelerated Carbonation and Properties of Artificial Steel Slag Aggregates. *Cem. Concr. Compos.* **2021**, *118* (December 2020). https://doi.org/10.1016/j.cemconcomp.2021.103948.

(23) Azdarpour, A.; Asadullah, M.; Mohammadian, E.; Hamidi, H.; Junin, R.; Karaei, M. A.

A Review on Carbon Dioxide Mineral Carbonation through PH-Swing Process. Chem. Eng. J. 2015, 279, 615–630. https://doi.org/10.1016/j.cej.2015.05.064.

(24) Bustillos, S.; Alturki, A.; Prentice, D.; La Plante, E. C.; Rogers, M.; Keller, M.; Ragipani, R.; Wang, B.; Sant, G.; Simonetti, D. A. Implementation of Ion Exchange Processes for Carbon Dioxide Mineralization Using Industrial Waste Streams. Front. Energy Res. 2020, 8 (December), 1–17. https://doi.org/10.3389/fenrg.2020.610392.

(25) Zhai, H.; Chen, Q.; Yilmaz, M.; Wang, B. Enhancing Aqueous Carbonation of Calcium Silicate through Acid and Base Pretreatments with Implications for Efficient Carbon Mineralization. *Environ. Sci. Technol.* 2023, *57*(37) 13808–13817. https://doi.org/10.1021/acs.est.3c03942

(26) Yin, S.; Aldahri, T.; Rohani, S.; Li, C.; Luo, D.; Zhang, G.; Yue, H.; Liang, B.; Liu, W. Insights into the Roasting Kinetics and Mechanism of Blast Furnace Slag with Ammonium Sulfate for CO2 Mineralization. Ind. Eng. Chem. Res. 2019, 58 (31), 14026–14036. https://doi.org/10.1021/acs.iecr.9b03109.

(27) Monasterio-Guillot, L.; Di Lorenzo, F.; Ruiz-Agudo, E.; Rodriguez-Navarro, C. Reaction of Pseudowollastonite with Carbonate-Bearing Fluids: Implications for CO2 Mineral Sequestration. Chem. Geol. 2019, 524 (May), 158–173. https://doi.org/10.1016/j.chemgeo.2019.06.011.

(28) Golubev, S. V.; Pokrovsky, O. S.; Schott, J. Experimental determination of the effect of dissolved CO2 on the dissolution kinetics of Mg and Ca silicates at 25 C. Chem. Geol. 2015, 217 (3-4), 227-238. https://doi.org/10.1016/j.chemgeo.2004.12.011

(29) Corradini, P.; Auriemma, F.; De Rosa, C. Crystals and Crystallinity in Polymeric Materials. Acc. Chem. Res. 2006, 39 (5), 314–323. https://doi.org/10.1021/ar040288n

(30) Wolff-Boenisch, D.; Gislason, S. R.; Oelkers, E. H. The Effect of Crystallinity on Dissolution Rates and CO2 Consumption Capacity of Silicates. Geochim. Cosmochim. Acta 2006, 70 (4), 858–870. https://doi.org/10.1016/j.gca.2005.10.016

(31) Criado, J.; Diane, M.; Macias, M.; PARADAS Bpro, M. C~Ystalli~ Sauces and Al Steins of Double Strontjum and Barium Carbonates. Elsevier Sci. Publ. B.V 1990, 171, 229–238.

(32) Li, Y.; Liu, W.; Xing, F.; Wang, S.; Tang, L.; Lin, S.; Dong, Z. Carbonation of the Synthetic Calcium Silicate Hydrate (C-S-H) under Different Concentrations of CO2: Chemical Phases Analysis and Kinetics. J. CO2 Util. 2020, 35 (November 2019), 303–

313. https://doi.org/10.1016/j.jcou.2019.10.001

(33) Ashraf, W.; Olek, J. Carbonation Behavior of Hydraulic and Non-Hydraulic Calcium Silicates: Potential of Utilizing Low-Lime Calcium Silicates in Cement-Based Materials. J. Mater. Sci. 2016, 51 (13), 6173–6191. https://doi.org/10.1007/s10853-016-9909-4

(34) Zhang, Z.; Wang, X.; Zhao, J. Phosphate Recovery from Wastewater Using Calcium Silicate Hydrate (C-S-H): Sonochemical Synthesis and Properties. Environ. Sci. Water Res. Technol. 2019, 5 (1), 131–139. https://doi.org/10.1039/c8ew00643a

(35) Lam, R. K.; Smith, J. W.; Rizzuto, A. M.; Karslloğlu, O.; Bluhm, H.; Saykally, R. J. Reversed Interfacial Fractionation of Carbonate and Bicarbonate Evidenced by X-Ray Photoemission Spectroscopy. J. Chem. Phys. 2017, 146 (9). https://doi.org/10.1063/1.4977046

(36) Reding, N. S.; Shiflett, M. B. Characterization of Thermal Stability and Heat Absorption for Suppressant Agent/Combustible Dust Mixtures via Thermogravimetric Analysis/Differential Scanning Calorimetry. Ind. Eng. Chem. Res. 2019, 58 (11), 4674–4687. https://doi.org/10.1021/acs.iecr.8b06143

(37) Zhai, H.; Wang, L.; Hövelmann, J.; Qin, L.; Zhang, W.; Putnis, C. V. Humic Acids Limit the Precipitation of Cadmium and Arsenate at the Brushite-Fluid Interface. Environ. Sci. Technol. 2019, 53 (1), 194–202. https://doi.org/10.1021/acs.est.8b05584.

(38) Walzak, M. J.; Davidson, R.; Biesinger, M. The Use of XPS, FTIR, SEM/EDX, Contact Angle, and AFM in the Characterization of Coatings. *J. Mater. Eng. Perform.* **1998**, *7* (3), 317–323. https://doi.org/10.1361/105994998770347747.

(39) Zhai, H.; Wang, L.; Qin, L.; Zhang, W.; Putnis, C. V.; Putnis, A. Direct Observation of Simultaneous Immobilization of Cadmium and Arsenate at the Brushite-Fluid Interface. Environ. Sci. Technol. 2018, 52 (6), 3493–3502. https://doi.org/10.1021/acs.est.7b06479

(40) Zhai, H.; Fan, Y.; Zhang, W.; Varsano, N.; Gal, A. Polymer-Rich Dense Phase Can Concentrate Metastable Silica Precursors and Regulate Their Mineralization. ACS Biomater. Sci. Eng. 2023. https://doi.org/10.1021/acsbiomaterials.2c01249

(41) Zhai, H.; Bernstein, R.; Nir, O.; Wang, L. Molecular Insight into the Interfacial Chemical Functionalities Regulating Heterogeneous Calcium-Arsenate Nucleation. J. Colloid Interface Sci. 2020, 575, 464–471. https://doi.org/10.1016/j.jcis.2020.04.126

(42) Hou, X.; Kirkpatrick, R. J.; Struble, L. J.; Monteiro, P. J. M. Structural Investigations

of Alkali Silicate Gels. J. Am. Ceram. Soc. 2005, 88 (4), 943–949. https://doi.org/10.1111/j.1551-2916.2005.00145.x

(43) Cong, X.; James Kirkpatrick, R. 29Si MAS NMR Study of the Structure of Calcium Silicate Hydrate. Adv. Cem. Based Mater. 1996, 3 (3–4), 144–156. https://doi.org/10.1016/s1065-7355(96)90046-2

(44) Chen, J. J.; Thomas, J. J.; Taylor, H. F. W.; Jennings, H. M. Solubility and Structure of Calcium Silicate Hydrate. Cem. Concr. Res. 2004, 34 (9), 1499–1519. https://doi.org/10.1016/j.cemconres.2004.04.034.

(45) Kellermeier, M.; Melero-Garcia, E.; Glaab, F.; Klein, R.; Drechsler, M.; Rachel, R.; García-Ruiz, J. M.; Kunz, W. Stabilization of amorphous calcium carbonate in inorganic silica-rich environments. *J. Am. Chem. Soc.* 2010, 132(50), 17859–17866. https://doi.org/10.1021/ja106959p

(46) Liu, Z.; Zhang, Z.; Wang, Z.; Jin, B.; Li, D.; Tao, J.; Tang, R.; De Yoreo, J.J., Shape-preserving amorphous-to-crystalline transformation of CaCO3 revealed by in situ TEM. Proc. Natl. Acad. Sci. U.S.A. 2020, 117(7), 3397-3404. https://doi.org/10.1073/pnas.1914813117

(47) Hou, X.; Kirkpatrick, R. J.; Struble, L. J.; Monteiro, P. J. M. Structural Investigations of Alkali Silicate Gels. J. Am. Ceram. Soc. 2005, 88 (4), 943–949. https://doi.org/10.1111/j.1551-2916.2005.00145.x

(48) Terry, B. The Acid Decomposition of Silicate Minerals Part I. Reactivities and Modes of Dissolution of Silicates. *Hydrometallurgy* **1983**, *10* (2), 135–150. https://doi.org/10.1016/0304-386X(83)90002-6

(49) Cama, J.; Ganor, J. The Effects of Organic Acids on the Dissolution of Silicate Minerals: A Case Study of Oxalate Catalysis of Kaolinite Dissolution. *Geochim. Cosmochim. Acta* **2006**, *70* (9), 2191–2209. https://doi.org/10.1016/j.gca.2006.01.028

(50) Geisler, T.; Dohmen, L.; Lenting, C.; Fritzsche, M. B. K. Real-Time in Situ Observations of Reaction and Transport Phenomena during Silicate Glass Corrosion by Fluid-Cell Raman Spectroscopy. *Nat. Mater.* **2019**, *18* (4), 342–348. https://doi.org/10.1038/s41563-019-0293-8

(51) Halasz, I.; Agarwal, M.; Li, R.; Miller, N. What Can Vibrational Spectroscopy Tell about the Structure of Dissolved Sodium Silicates? *Microporous Mesoporous Mater.* **2010**, *135* (1–3), 74–81. https://doi.org/10.1016/j.micromeso.2010.06.013.

(52) Zhu, G.; Legg, B. A.; Sassi, M.; Liang, X.; Zong, M.; Rosso, K. M.; De Yoreo, J. J. Crystal Dissolution by Particle Detachment. Nat. Commun. 2023, 14 (1), 1–11. https://doi.org/10.1038/s41467-023-41443-y.

(53) Schott, J.; Pokrovsky, O. S.; Spalla, O.; Devreux, F.; Gloter, A.; Mielczarski, J. A. Formation, growth and transformation of leached layers during silicate minerals dissolution: The example of wollastonite. Geochim. Cosmochim. Acta 2012, 98, 259−281. https://doi.org/10.1016/j.gca.2012.09.030

(54) Molster, F.; Kemper, C., Crystalline silicates. *Space Sci. Rev.*, 2005, 119, 3-28. https://doi.org/10.1007/s11214-005-8066-x